Numerical Modeling of Interaction of Turbulent Flow with a Buried Circular Cylinder on a Plane Surface

M. Sami AKÖZ[1]
Oğuz ŞİMŞEK[2]
N. Göksu SOYDAN[3]

ABSTRACT

Turbulent flow characteristics around a partially buried horizontal circular cylinder are investigated numerically for the burial ratio of B/D=0.50 (B is burial depth, D is the diameter of the cylinder). The governing equations are numerically solved using ANSYS-Fluent for the flows having the same conditions with the experiments related to measurements of velocity field by Particle Image Velocimetry for Reynolds numbers based on the cylinder diameter, in the ranges of $1000 \leq Re_\mathrm{D} \leq 7000$. Standard k-ε, Renormalization-group k-ε, Realizable k-ε, Modified k-ω, Shear Stress Transport k-ω and Reynolds Stress turbulence models are employed. Experimental validations of the numerical results show that Shear Stress Transport k-ω model provides better predictions for the kinematic properties of the turbulent flow than the other turbulence models used herein. Force coefficients also predicted numerically at Reynolds numbers in the ranges of $1000 \leq Re_\mathrm{D} \leq 7000$ for the burial ratio, B/D=0, 0.25 and 0.5.

Keywords: Buried cylinder, force coefficients, PIV, turbulence models, turbulent flow.

1. INTRODUCTION

Turbulent flow around bluff bodies, especially cylinders, has been studied extensively because of an important subject encountered in many engineering applications. When a cylindrical structure is installed on an erodible bed such as submarine pipelines, interaction of the turbulent flow with the floor may create erosion that causes problems such as instability of the structure. The horse shoe vortex around the structure and down-flow that results from the downward hydraulic gradient in front of the structure contribute significantly to the scour.

Following the propagation of the scour along the pipeline, it can lead to bearing failure and self-weight settlement of the pipeline and subsequently the pipeline may be covered by sand and presumably be self-buried [1]. In spite of the fact that the processes of scouring and self-burial of the pipelines are governed by various mechanisms, they depend mostly on the hydrodynamic behavior of the flow around the pipeline. Therefore, a deeper physical understanding of vortical flow structure is very important for stability of the structure. There are a number of experimental studies in the literature for the analysis of the flow characteristics around a cylindrical structure [2, 3, 4, 5, 6, 7, 8, 9]. The primary interests in these and related studies include measurements of the distribution of pressure around a cylinder, analysis of vortex shedding mechanisms and consequently obtaining the Strouhal number, investigation of the wall-proximity effects on the hydrodynamic forces, description of the mechanisms of scour and self-burial process and visualization of the turbulent flow structures around the cylindrical structure.

With the rapid development of computers and computational fluid dynamics (CFD) in recent years, a number of numerical simulations of the turbulent flow interaction with bluff bodies and scour process have been conducted. Olsen and Kjellesvig [10], modeled numerically in three-dimensional flow around a circular cylinder placed vertically in a flume. In the numerical modeling of $3D$ turbulence flow, the governing equations were solved by k-ε turbulence closure model. They found that the calculated maximum scour depth corresponds reasonably well with empirical formulas and other calculated flow characteristics such as the development of the scour hole, the shape of the scour hole and the water surface elevation around the cylinder correspond well with observations from physical model studies. Liang, Cheng and Li [11], developed a vertical two-dimensional numerical model for time dependent local scour below offshore pipelines subject to unidirectional steady flow. They examined the performance of two turbulence models, the standard k-ε model and Smagorinsky sub-grid scale (SGS) model, on modeling time dependent scour processes. From the comparisons of the predicted and measured scour-hole profiles, it is found that the proposed model works well for both clear-water and live-bed scour situations and the k-ε turbulence closure model is more preferable regarding the SGS model in the $2D$ scour model. Zhao and Fernando [12], used an Eulerian two-phase model embedded in FLUENT software to simulate scour around pipelines on a sandy bed. They used k-ε turbulence closure model for the fluid phase in the numerical model. Their simulation results were validated using experimental data by Mao [13]. They reported that the quantitative results on scour depth (time) evolution and the maximum scour depth agree well with the experimental results. Kirkgoz, Oner and Akoz [14], carried out the numerical simulation of $2D$ turbulent flow around a horizontal circular cylinder near a rigid bed with gap ratio $G/D = 0.3$ at Reynolds number based on cylinder diameter Re_D= 9500. The governing equations were solved by k-ε, k-ω and Shear Stress Transport (SST) k-ω turbulence closure models. It was reported that the shedding of vortices in the cylinder wake was not predicted by k-ε model and the numerical modeling using either k-ω and SST k-ω turbulence models were reasonably successful. Akoz and Kirkgoz [15], investigated numerically the turbulent flow around a horizontal wall-mounted circular cylinder at Reynolds numbers in the range of $1000 \leq Re_D \leq 7000$. The flow field was solved using k-ε, k-ω and SST turbulence models. By comparing the experimental and numerical results it was found that the velocity field obtained using k-ω and SST turbulence models were generally more accurate than k-ε model. Dixen, Sumer and Fredsoe [16], investigated the flow and scour around a half-buried sphere exposed to a

steady current experimentally and numerically. They compared experimental findings obtained by the hot-film and Laser Doppler Anemometer measurements with the numerical results obtained using k-ω SST turbulence closure model. They reported that the scour depth increases and time scale decreases when the effect of externally-generated turbulence is incorporated in the calculations and the equilibrium maximum scour depth in the live-bed regime can be approximated by $0.5D$ in which D is the sphere diameter. Zhu, Qi, Lin and Yang [17], performed a numerical study on the flow field around a submarine pipe equipped with a spoiler in a rectangular configuration and the variation of seabed surface caused by current-induced scouring beneath the pipe. Euler–Euler two-phase flow model was employed to capture the flow characteristics of sea water and seabed sandy particles based on two-dimensional Reynolds-Averaged Navier–Stokes (RANS) equations using the SST k-ω turbulence model. Their numerical results showed that both flow field around submarine pipe and seabed scouring were sensitive to the relative spoiler height and gap ratio. Increasing the spoiler height or decreasing the gap ratio could accelerate the self-burial process for submarine pipe equipped with a spoiler.

Further studies on the numerical analysis of the flow around the buried cylinders or cylinders over a scoured bed using different turbulence models for different flow conditions would be useful to experimentally validate and enhance the reliability of the CFD simulations for scour and self-burial mechanisms. In this study, the turbulent characteristics of flow around a partially buried horizontal circular cylinder located at the bottom of the channel are investigated numerically for Reynolds numbers in the range of $1000 \leq Re_D \leq 7000$. Firstly, in order to determine the most successful turbulence model, the governing equations are solved numerically by ANSYS-Fluent software using; Standard k-ε (SKE), Renormalization-group k-ε (RNG), Realizable k-ε (RKE), Modified k-ω (MKW), Shear Stress Transport k-ω (SST) and Reynolds Stress Model (RSM) for flow condition of $Re_D = 5000$. Secondly, the numerical results using the most successful turbulence models are compared with PIV measurements by Aköz [9] for Reynolds numbers, in the range of $1000 \leq Re_D \leq 7000$ based on the cylinder diameter. Turbulence characteristics of the flow field and coefficients of forces exerted on the cylinder are also presented for $1000 \leq Re_D \leq 7000$.

2. EXPERIMENTAL SET-UP

The numerical model validation was achieved against the experimental data by Aköz [9] (Fig.1). Experiments were performed in a closed-loop water channel test-section. The channel, made of transparent Plexiglas with 15 mm thickness, is 8.0 m in length, 1.0 m in width and 0.75 m in height. During the experimental study, the height of water (h) was 0.45 m and Reynolds numbers based on the cylinder diameter were $Re_D = 1000, 3000, 5000$ and 7000. The different Reynolds numbers were obtained by changing the flow velocity. A smooth circular cylinder having the burial ratio as $B/D = 0.50$, was mounted horizontally on the channel surface, in which B is burial depth, D is the diameter of the cylinder. The diameter and height of the cylinder were 30 mm and 15 mm respectively for $B/D = 0.50$. The Digital Particle Image Velocimetry (PIV) technique was employed to obtain the instantaneous velocity vector field around the partially buried circular cylinder. The flow field illumination was provided by two Nd: Yag laser sources of a wavelength of 532 nm, each with a maximum energy output of 120 mJ. Dantec Dynamics Processor, which was controling the timing of the data acquisition, was used to synchronize the image taking and laser unit. In each

experiment, 300 instantaneous images at 15 Hz frequency were captured, recorded and stored in order to obtain averaged-velocity vectors and other statistical properties of the flow field. More details for PIV measurements may be found in Aköz [9].
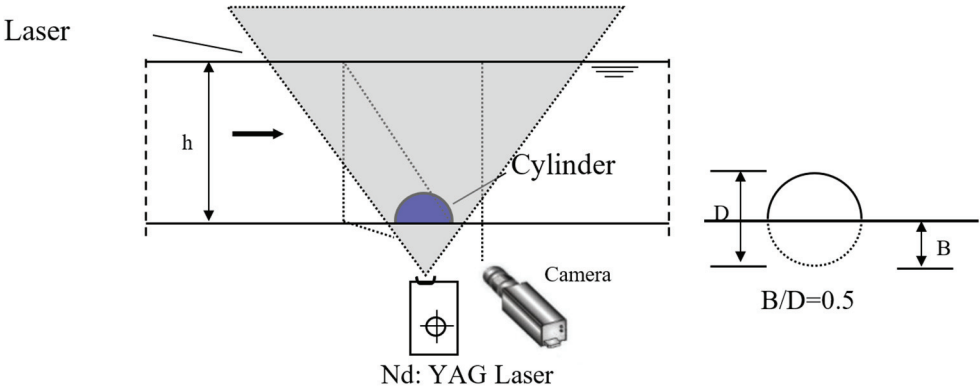
Figure 1 - Experimental setup (Aköz [9])

3. NUMERICAL MODELING

3.1. Governing Equations and Turbulence Closure Models

2-D Reynolds-averaged continuity and Navier-Stokes equations (RANS) are used to theoretically simulate the present open channel flow over a partially buried circular cylinder. For an incompressible, Newtonian fluid flow these equations can be expressed as

$$\frac{\partial \bar{u}_i}{\partial x_i} = 0 \tag{1}$$

$$\rho \left(\frac{\partial \bar{u}_i}{\partial t} + \bar{u}_j \frac{\partial \bar{u}_i}{\partial x_j} \right) = \rho g_i - \frac{\partial \bar{p}}{\partial x_i} + \mu \frac{\partial^2 \bar{u}_i}{\partial x_j^2} + \frac{\partial \tau_{ij}}{\partial x_j} \tag{2}$$

In Eqs. (1) and (2), u_i is the velocity component in x_i-direction, g_i is gravity, p is pressure, μ is dynamic viscosity, ρ is fluid density, t is time, $\tau_{ij}(=-\rho \overline{u_i' u_j'})$ is the turbulence stresses. The turbulence stresses are obtained from the linear constitutive equation formulated by Boussinesq

$$\tau_{ij} = -\rho \overline{u_i' u_j'} = \mu_t \left(\frac{\partial \bar{u}_i}{\partial x_j} + \frac{\partial \bar{u}_j}{\partial x_i} \right) - \frac{2}{3} \rho k \delta_{ij} \tag{3}$$

In Eq. (3) u_i' and u_j' are the horizontal and vertical velocity fluctuation component, respectively, μ_t is turbulent viscosity, k ($= \overline{u_i'u_i'}/2$) is turbulent kinetic energy and δ_{ij} is Kronecker delta. The models used for the turbulent viscosity in Eq. (3) are briefly described in the following. To determine the turbulent viscosity μ_t in Eq. (3), turbulence closure models given below were used.

> **1.** Standard k-ε (SKE) [18],
>
> **2.** Renormalization-group k-ε (RNG) [19],
>
> **3.** Realizable k-ε (RKE) [20],
>
> **4.** Modified k-ω (MKW) [21],
>
> **5.** Shear Stress Transport k-ω (SST) [22],
>
> **6.** Reynold Stress Model (RSM) [23].

3.2. Solution Domain and Boundary Conditions

The conditions for numerical simulations were made to be the same as those used in the experiment. The computational domain that its height is equal to 15*D,* extends 50*D* downstream and 20*D* upstream, above, and below the cylinder (Fig.2). At the inflow boundary, the vertical distributions of the horizontal velocity components were assumed to be uniform $u=u_0$ and the vertical velocity component as $v=0$. The uniform horizontal velocity components are u=33.3, 100.0, 166.7 and 233.3 mm/s for Re_D=1000, 3000, 5000 and 7000, respectively. All solid walls were defined as the wall boundary condition in which no-slip condition is imposed i.e., u=0, v=0. On the top boundary of the domain, symmetric conditions are imposed, i.e. normal gradients of velocity are set to zero on the boundary. At the outflow boundary p=0 was used.

u=33.3-233.3 mm/s
v=0 mm/s
Flow direction
15*D*
p=0
50*D*
D
20*D*
u=0, *v*=0
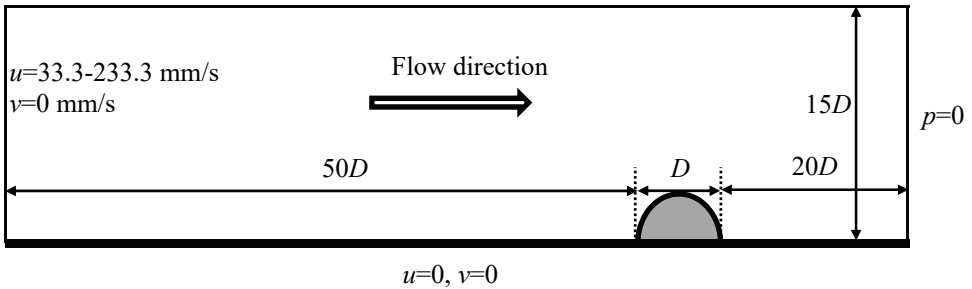
Figure 2 - Geometry and boundary conditions of computational domain

Considering the low turbulence characteristics of the flow at the inflow boundary, the turbulent intensity was accepted to be 0.01. The fluctuating velocity component v' at the

inflow boundary was assumed to have the magnitude of the inlet velocity v times the inlet intensity, and the turbulence length scale was calculated as the hydraulic diameter multiplied by the inlet scale factor. In the numerical modeling the transient analyses were performed. From the experimental measurements the turbulence intensity and the hydraulic diameter were obtained as 1% and 0.2368, respectively under flow condition at Re_D=7000. In the inlet boundary condition of the numerical modeling these parameters were used. The iteration number in the numerical analyses was given as 10 while the time step size was 0.001. The solution time was taken as 60 seconds for all analyses, which is determined by the provisions of the continuity equilibrium.

3.2.1. Near-wall treatment

In this study, two-layer approach was applied for resolving the near wall region. In this approach, the whole domain is subdivided into a fully-turbulent region and a viscosity affected region. In the fully turbulent region, k-ε, k-ω models and RSM model are employed. In the viscosity-affected region (the viscous sublayer and the buffer layer), the one equation-model of Wolfshtein [24] is employed with extremely fine grids and no slip conditions (i.e. u=v=0). Two-layer formulation of turbulent viscosity is smoothly blended with high Re-number definition for μ_t from outer region. A similar procedure is applied in order to ensure a smooth transition between the algebraically specified ε ($=k^{3/2}/l_e$, where l_e is the length scale) in the viscosity affected region and ε obtained from the solution of the transport equation, in the outer region.
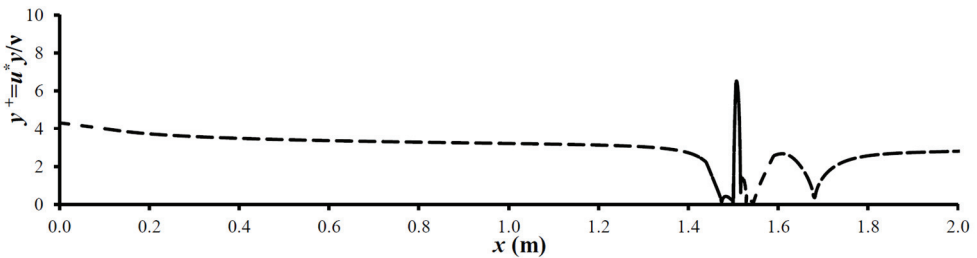
Figure 3 - The variation of y^+ ($=v_*y/v$) value along the solid boundary

The size of the wall adjacent cell should be so adjusted that it is embedded in the viscous sublayer where the linear viscous relation takes place between the dimensionless velocity u^+ ($=u/v_*$) and dimensionless distance y^+ ($=v_*y/v$), in which y is the distance normal to the wall, v_*=(τ_0/ρ)$^{1/2}$ is the shear velocity and τ_0 is boundary shear stress. Kirkgoz and Ardiclioglu [25], reported that the experimental data fit the linear velocity distribution in the viscous sublayer if y^+≤10. This result was used as a criterion to evaluate the adequacy of the near-wall mesh size for the two layers model. The mesh resolution was therefore adjusted to have the first mesh point within the viscous sublayer by keeping the near-wall mesh size normal to the solid bed within the limit of y^+≤10. Fig.3 shows the variation of y^+ ($=v_*y/v$) value along the channel and on the buried cylinder surface obtained by using the SST turbulence model

for the fine mesh under flow condition at Re_D=7000. As shown in the figure, the maximum value of y^+ takes place on the backward shoulder of the buried cylinder and its value is less than 10. It is also seen that the y^+ values in the subcritical and supercritical region are below 2.

3.3 Computational Meshes

3.3.1. Mesh Design

Fig. 4 shows the computational grid used for the numerical solutions. As seen in the figure, solution domain is divided into 10 sub-domains with four-node quadrilateral elements. Considering the characteristics of the flow within the solution domain, relatively compressed meshes were used toward the solid boundaries (i.e. near the cylinder surface and the plane wall) to improve the prediction accuracy for the shear layer region where the velocity gradient is high. Table 1 gives the element numbers of the three mesh systems used for computations. In this study the mesh orthogonal skewness is obtained as 0.399. If the value is between 0.25 and 0.50, cell quality is defined as good. The range for orthogonal quality is 0-1, where a value of 0 is worst and a value of 1 is best [26]. The minimum orthogonal quality is obtained as 0.610 in the present study.
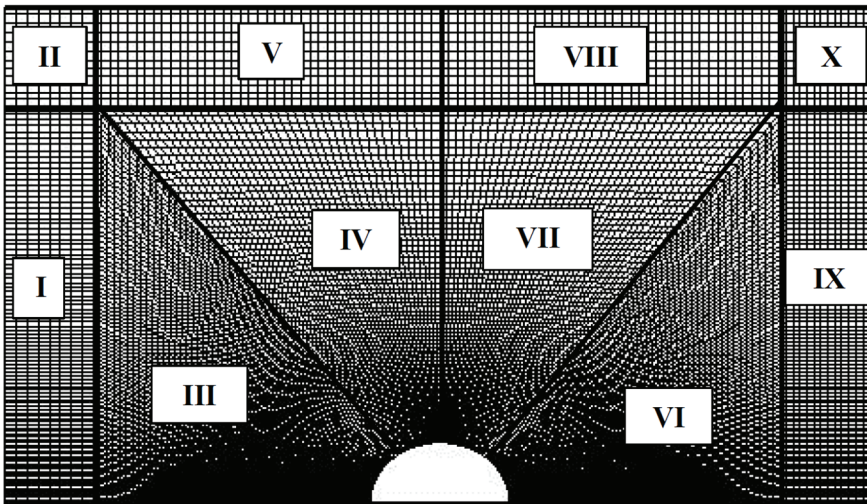
Figure 4 - Sub-domains of computational grid

Table 1 - Element numbers of the three mesh systems used for computations

Sub-domains of three meshes	Mesh 1 (coarse)	Mesh 2 (medium)	Mesh 3 (fine)
I	40x50	60x75	80x100
II	40x40	60x60	80x80

Table 1 - Element numbers of the three mesh systems used for computations (continue)

Sub-domains of three meshes	Mesh 1 (coarse)	Mesh 2 (medium)	Mesh 3 (fine)
III, IV	40x40	60x60	80x80
V	40x50	60x75	80x100
VI	50x75	75x100	100x150
VII	50x5	75x5	100x10
VIII, IX	40x5	60x5	80x10
X	75x5	100x5	150x10
Total number of mesh elements	11,775	24,875	47,100

3.3.2. Estimation of discretization error

A grid convergence index (GCI) was determined for the computed velocities on the three meshes, which is the most common and reliable technique for the quantification the discretization uncertainty of the numerical results [27]. Using the Richardson error estimator to compare the three grids, the fine-grid convergence index is defined as

$$\text{GCI}_{23}^{\text{fine}} = \frac{1.25|E_{23}|}{r_{23}^{P} - 1} \tag{4}$$

where $E_{23} = (u_{s3} - u_{s2})/u_{s3}$ = approximate relative error between the medium and fine meshes, u_{s2} and u_{s3} = medium and fine mesh solutions for velocities obtained with grid spacing d_2 and d_3, respectively, and P = local order of accuracy. For the three-grid solutions, P is obtained by solving the equation

$$P = \frac{1}{\ln r_{23}} \ln \frac{(r_{23}^{P} - 1)e_{12}}{(r_{12}^{P} - 1)e_{23}} \tag{5}$$

in which $e_{12} = u_{s1} - u_{s2}$, $e_{23} = u_{s2} - u_{s3}$, and $r_{12} = d_1/d_2$ and $r_{23} = d_2/d_3$ = grid refinement factors between coarse and medium, and medium and fine grid, respectively. For the present comparisons $d_3 < d_2 < d_1$.

In this study, the profiles of computed velocities u at x=1.45, 1.515 and 1.60 m were used to determine the numerical uncertainties due to discretization. Table 2 shows the discretization uncertainty for the fine-grid solutions using the SST turbulence model. Note that the maximum uncertainty in the chosen velocity profiles on Mesh 3 is 1.959% corresponding to ±0.0129 m/s at x=1.60 and y=0.008 m. As it is seen from Table 2, the numerical uncertainty of discretization in the computed velocities for Mesh 3 remains within 2% which is an excellent indication.

Table 2 - Sample error estimates in velocity profiles at x=1.45, 1.515 and 1.60 m.

x=1.45 m		*x*=1.515 m		*x*=1.60 m	
y (m)	$\mathrm{GCI}_{23}^{\mathrm{fine}}$ for *u* (%)	*y* (m)	$\mathrm{GCI}_{23}^{\mathrm{fine}}$ for *u* (%)	*y* (m)	$\mathrm{GCI}_{23}^{\mathrm{fine}}$ for *u* (%)
0.000	0.747	0.016	0.928	0.001	1.280
0.002	1.363	0.017	1.166	0.005	0.040
0.004	-1.937	0.019	-1.909	0.008	1.959
0.008	0.671	0.020	0.119	0.010	1.819
0.012	1.849	0.021	0.016	0.012	0.473
0.016	0.190	0.022	0.829	0.014	1.938
0.020	-0.899	0.023	0.998	0.016	1.850
0.024	0.070	0.024	0.070	0.018	0.005
0.028	0.071	0.026	0.376	0.021	1.368
0.032	0.376	0.028	1.095	0.025	0.004
0.036	0.980	0.030	-1.395	0.030	-1.504
0.040	0.102	0.032	-1.783	0.032	-1.391

4. EXPERIMENTAL AND COMPUTATIONAL RESULTS

4.1. Experimental and Computed Velocity Profiles

A quantitative evaluation of the measured and computed velocity comparisons was made by the mean absolute relative error (MARE)

$$MARE = \frac{1}{N} \sum_{n=1}^{N} \left| \frac{\bar{u}_m - \bar{u}_c}{\bar{u}_m} \right| x100 \tag{6}$$

in which $\bar{u}_m$ and $\bar{u}_c$ are the measured and computed horizontal velocities, respectively and *N* is the total number of data on the velocity profiles. The results for MARE using Eq. (6) for the horizontal velocity profiles at different channel sections for Re_D=5000 were given in Table 3 for all turbulence closure models used in the present study. The numbers in parentheses in the table indicate the order of success in regard to compliance with the experimental measurements. SKE model shows superior performance in the upstream and upper region of the buried cylinder except for the upstream separation region in front of the cylinder as expected. In the upstream separation region, SST turbulence model performs better than the others. However, the results using the MKW and RSM are very close to those of the SST in this region. SKE, RNG and RKE turbulence models give very poor results in the downstream region of the cylinder especially in the near wake region. SST model shows better agreement at *x/D*=0.5 in the near wake region. RSM model provides better estimations

of horizontal velocity component far away from the cylinder when compared to the others. On the other hand, in terms of the mean MARE values, the SST turbulence model gives the best predictions which are followed by the MKW and RSM models.

Table 3 - MARE values for the horizontal velocity profiles at different sections for the turbulence models

x/D	SKE	RNG	RKE	MKW	SST	RSM
-1.5	**6.35**[1]	6.50[3]	6.43[2]	10.15[6]	10.01[5]	8.28[4]
-1.0	**9.18**[1]	9.36[3]	9.34[2]	13.63[6]	13.48[5]	10.90[4]
-0.5	29.17[6]	28.45[5]	28.14[4]	23.10[2]	**20.52**[1]	27.11[3]
0.0	**5.02**[1]	5.17[2]	5.21[3]	9.10[6]	8.59[5]	7.48[4]
0.5	236.56[6]	206.65[5]	164.21[4]	51.35[2]	**46.23**[1]	97.45[3]
1.0	95.77[6]	84.62[5]	66.77[4]	39.49[3]	23.53[2]	**19.24**[1]
1.5	82.08[6]	68.93[5]	45.75[4]	42.33[3]	34.47[2]	**25.56**[1]
Mean	66.31[6]	58.53[5]	46.55[4]	27.02[2]	**22.40**[1]	28.00[3]

The graphical comparisons of the horizontal velocity profiles between the experimental data and numerical predictions using the turbulence models for Re_D=5000 were also given in Figure 5. It can be seen clearly that while SST model shows better agreement with the experimental measurements at x/D=-0.5 and $x/D = 0.5$, SKE model gives superior results to the other models at x/D=0.
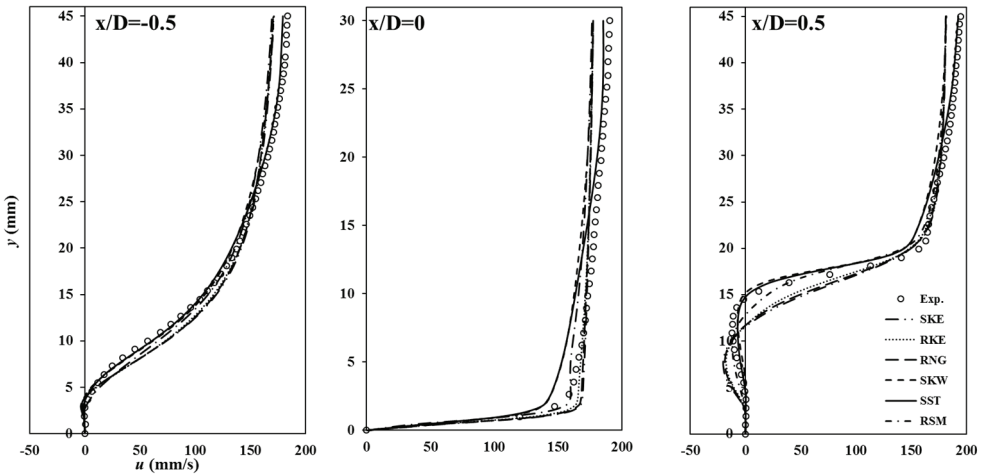
Figure 5 - Comparisons of measured and computed horizontal velocity profiles obtained by the present turbulence models at three different sections for Re_D=5000

Figure 6 shows the measured and predicted horizontal velocity profiles obtained by the most successful turbulence model (SST) regarding the mean MARE values on Mesh 3 at different channel sections for Reynolds numbers in the range of $1000 \leq Re_D \leq 7000$. The agreement appears to be very good between the experimental data and predictions of SST turbulence model. The largest discrepancies of SST predictions take place in the wake region of the cylinder. It is also seen that SST model predicts successfully the upstream and downstream separation region of the buried cylinder.
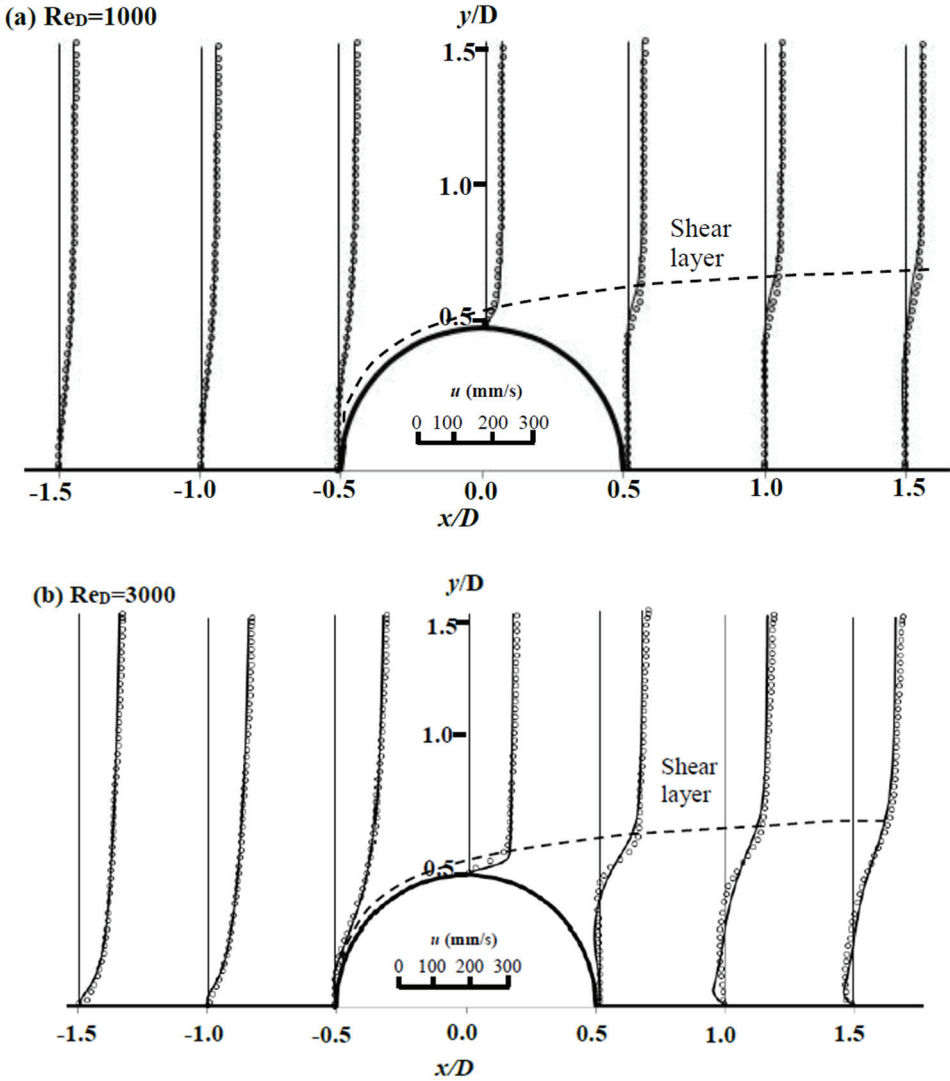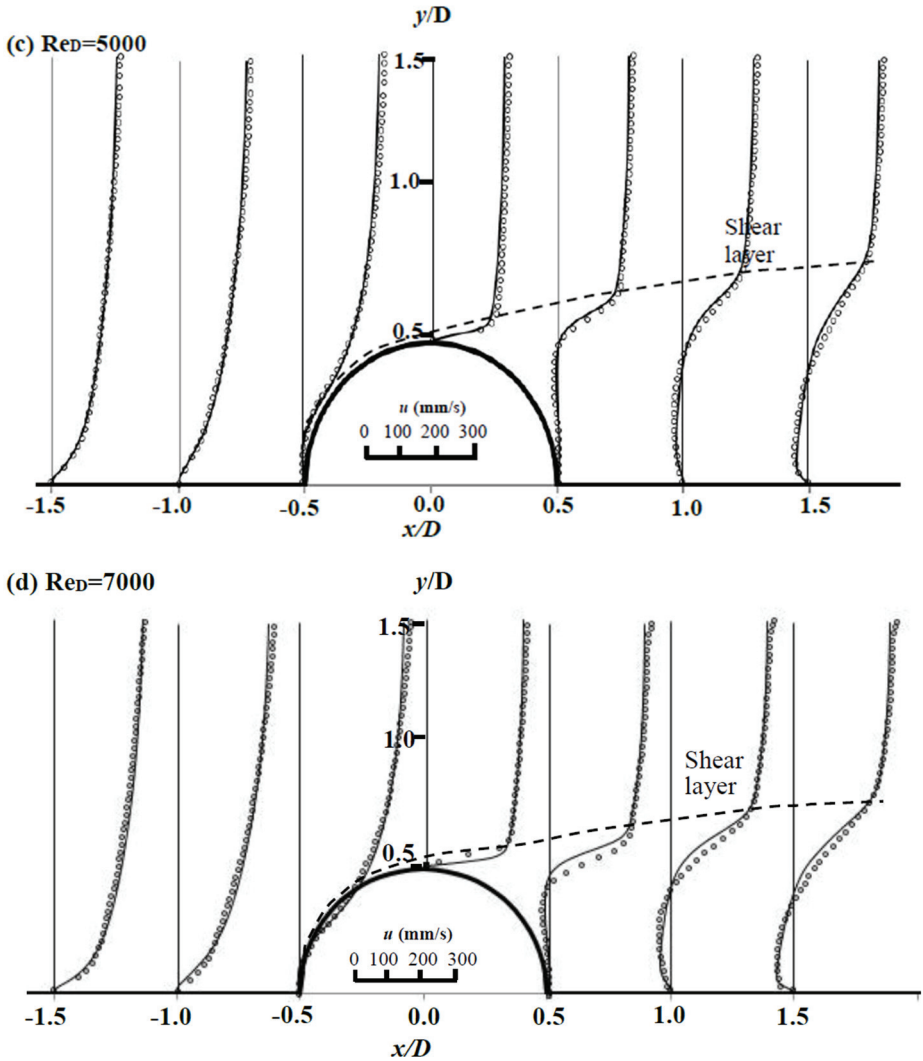
Figure 6 - Measured and computed horizontal velocity profiles using SST model at different channel sections for $1000 \leq Re_D \leq 7000$

4.2 Experimental and numerical streamlines and velocity vectors

Since SKE model is the most unsuccessful turbulence model as compared to the others to predict the velocity data at $x/D = -0.5$ and $x/D = 0.5$, as seen in Table 3, it should not be expected to provide accurately the separation region upstream and downstream of the cylinder. Therefore, in Figure 7 and 8, the comparisons of the experimental and numerical averaged patterns of corresponding streamline topology and velocity vectors in the upstream and downstream of the buried cylinder obtained using other five turbulence models were

presented for flow condition at Re_D=5000, respectively. It can be seen from the first columns of the figure that the computed length of the separation region in the upstream of the cylinder is overpredicted in the present simulations. However, reasonable predictions for the separation region in the upstream region of the buried cylinder were obtained except for RSM which predicted two reattachment points on the channel floor. RKE, RNG, MKW and SST predict almost identical location of separation point, S_s (approximately 1.5D) upstream of the cylinder. The numerical length of the separation regions upstream of the buried cylinder were predicted to be 1.02D, 0.92D, 0.83D and 0,78D for the RKE, RNG, MKW and SST, respectively. On the other hand, the experimental distance of S_s was determined to be approximately 0.54D. It can be also easily seen from the figures that a focus (F) that corresponds to vortex centers takes place between the separation point and forward face of the cylinder. The size of the vortices in the upstream region obtained using the present turbulence models is larger than the experimental result. The time-averaged distributions of the velocity vectors given in the last columns of the Figure 8 also reveal identical flow structures around the buried cylinder.

There are two separation regions called primary separation region which occurs in the downstream of the cylinder and secondary downstream separation region which is apparent in the near wake of the cylinder [13]. The second column of the Figure 7 shows the predicted time-averaged patterns of streamline in the downstream region of the buried cylinder. As can be seen in the figure, while the experimental length of the secondary downstream separation region was obtained as 0.40D, the numerical lengths of the secondary downstream separation regions were predicted to be 0.24D, 0.22D, 0.83D, 0,49D, and 0.25D for the RKE, RNG, MKW, SST and RSM, respectively. As can be understood from these values, SST model is the most successful turbulence model in predicting the flow structure around the buried cylinder.

Figure 9 shows the experimental and numerical time-averaged patterns of streamline topology obtained using the most successful turbulence model, SST for Reynolds numbers Re_D=1000, 3000, 5000 and 7000. For Re_D=1000, a vortex cluster does not appear in the experimental time-averaged streamline patterns upstream and downstream of the cylinder, while it does not take place only downstream of the cylinder in the numerical time-averaged streamline patterns. A possible reason is that the separation/boundary layer developing over the cylinder is not fully turbulent (transitional) in this case, whereas numerical model cannot sense such regimes due to the inherence of two-equation RANS closure used. As may be seen from the figure, SST model provides slightly longer separation regions in both upstream and downstream of the buried cylinder compared to the measurement ones for $1000 \leq Re_D \leq 7000$. Similar to the experiments, the length of the separation regions decreases with increasing Reynolds number. Also, the vortex in the junction region of the cylinder and channel bed weakens for increasing Reynolds number, as seen in Figure 9. This is because core flow easily penetrates into the wake region in the upstream and downstream of the buried cylinder due to the higher momentum at higher Reynolds number. Table 4 gives the comparison of boundary layer separation angles for B/D=0, B/D=0.25 and B/D=0.5 obtained by using SST turbulence model with the experimental measurements of Akoz [9] for $1000 \leq Re \leq 7000$. It can be said that as the Reynolds number increases for $1000 \leq Re \leq 7000$, boundary layer separation angles using SST turbulence model and PIV decreases. Akoz [9] analyzed the boundary layer separation angles for B/D=0 at Re_D=5000 by using SST turbulence model. The results for Re_D=5000 given in Table 4 are compatible with the values given by Akoz [9].
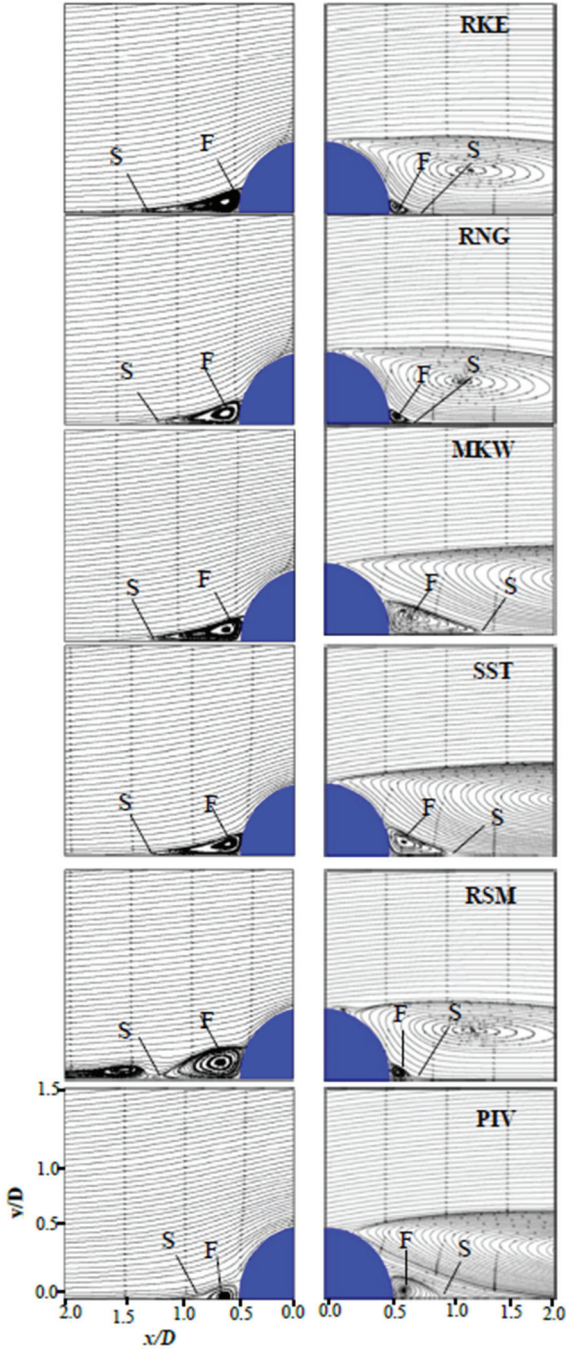
Figure 7 - Experimental and numerical time averaged patterns of streamlines for
$Re_D=5000$
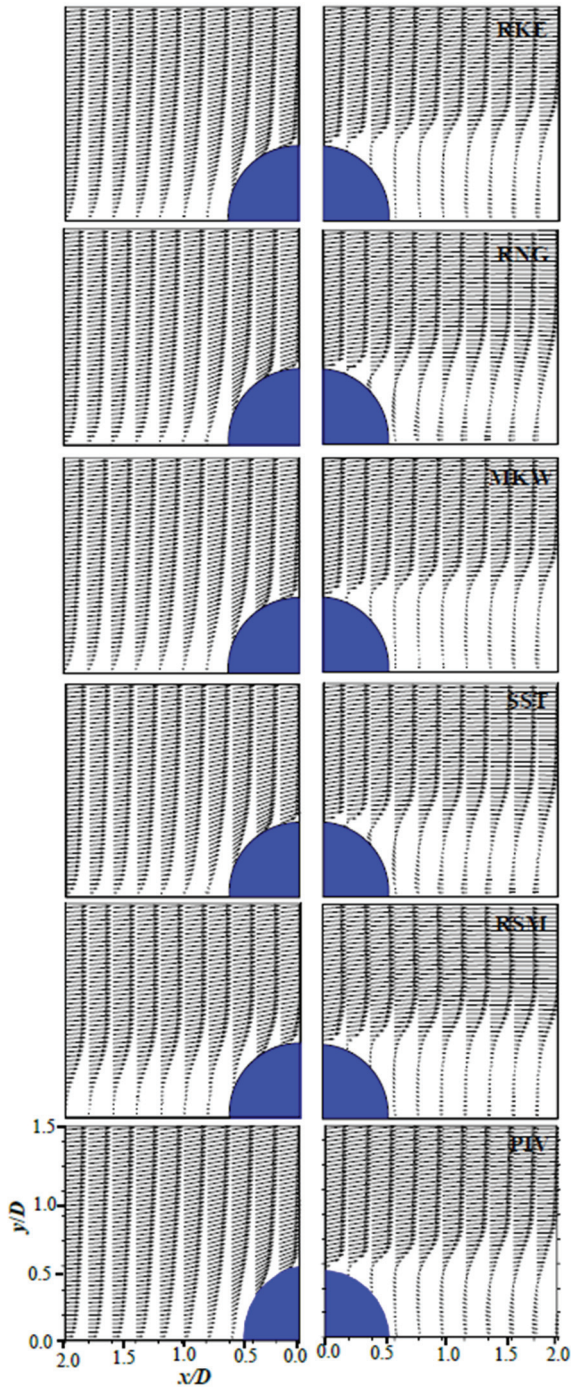
Figure 8 - Experimental and numerical distribution of velocity vectors for Re$_D$=5000
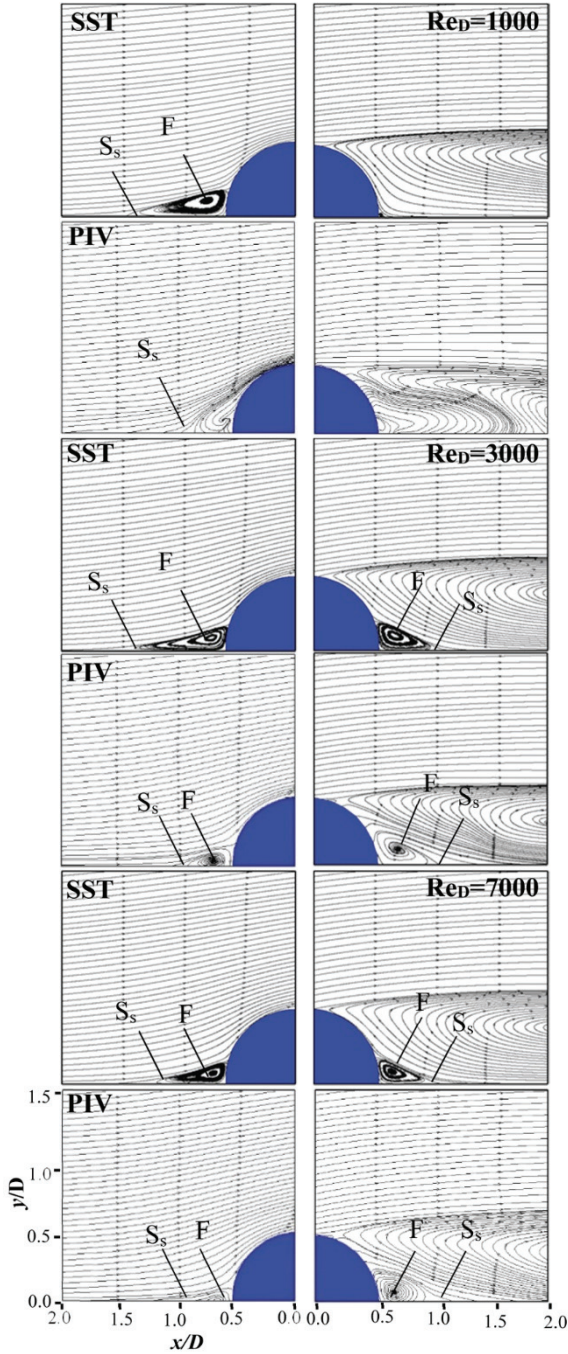
Figure 9 - Experimental and numerical time-averaged streamline patterns for
1000≤Re_D≤7000

Table 4 - Experimental and numerical boundary layer separation angles for B/D=0, B/D=0.25 and B/D=0.5

Re_D-B/D	SST			PIV		
	0	**0.25**	**0.5**	**0**	**0.25**	**0.5**
1000	120	118	123	104	107	112
3000	112	116	111	98	99	109
5000	106	108	108	98	97	104
7000	103	107	107	98	98	104

4.3. Force Coefficients

Figure 10 depicts the pressure coefficient, C_p distribution on the cylinder for B/D=0, 0.25 and 0.5 at Reynolds numbers in the ranges of $1000 \leq Re_D \leq 7000$. The pressure in the wake region is negative due to the flow separation. The characteristic of the pressure distribution for Re_D=1000 differs slightly from others and its pressure values are very small compared to other Reynolds numbers. Positive and negative C_p values are increasing with the increase of Reynolds number. The maximum values of pressure coefficient take place in the upstream of the cylinder. The point where the pressure passes from the positive to negative is almost the same point on the cylinder surface for all Reynolds numbers except for Re_D=1000, its starting point moves further downstream for Re_D=1000. The minimum values of C_p occur on the front shoulder of the cylinder. Its locations are between θ=70° and 90° for $0 \leq B/D \leq 0.50$ and they move slightly in the backward direction as the buried ratio increases. Table 5 gives the maximum negative values of C_p for B/D=0, B/D=0.25 and B/D=0.5. In addition, as the buried ratio, B/D is increased, the absolute value of pressure coefficient is decreased. This is consistent with the experimental data of pressure distribution around a cylinder for different buried pipe position by Cokgor and Avci [28].

Table 5 - The maximum negative values of Cp for B/D=0, B/D=0.25 and B/D=0.5

B/D-Re_D	1000	3000	5000	7000
0	-2.291	-2.417	-2.477	-2.813
0.25	-2.136	-2.363	-3.061	-3.543
0.5	-1.466	-1.692	-1.763	-2.031

The pressure, drag and lift coefficients for the forces acting on the cylinder were calculated. The drag and lift force coefficients, C_d and C_l, are

$$C_d = \frac{F_d}{\frac{1}{2}\rho u_0^2 D} \tag{7}$$

$$C_l = \frac{F_l}{\frac{1}{2}\rho u_0^2 D} \tag{8}$$

where the drag and lift forces, F_d and F_l, per unit length on the cylinder are
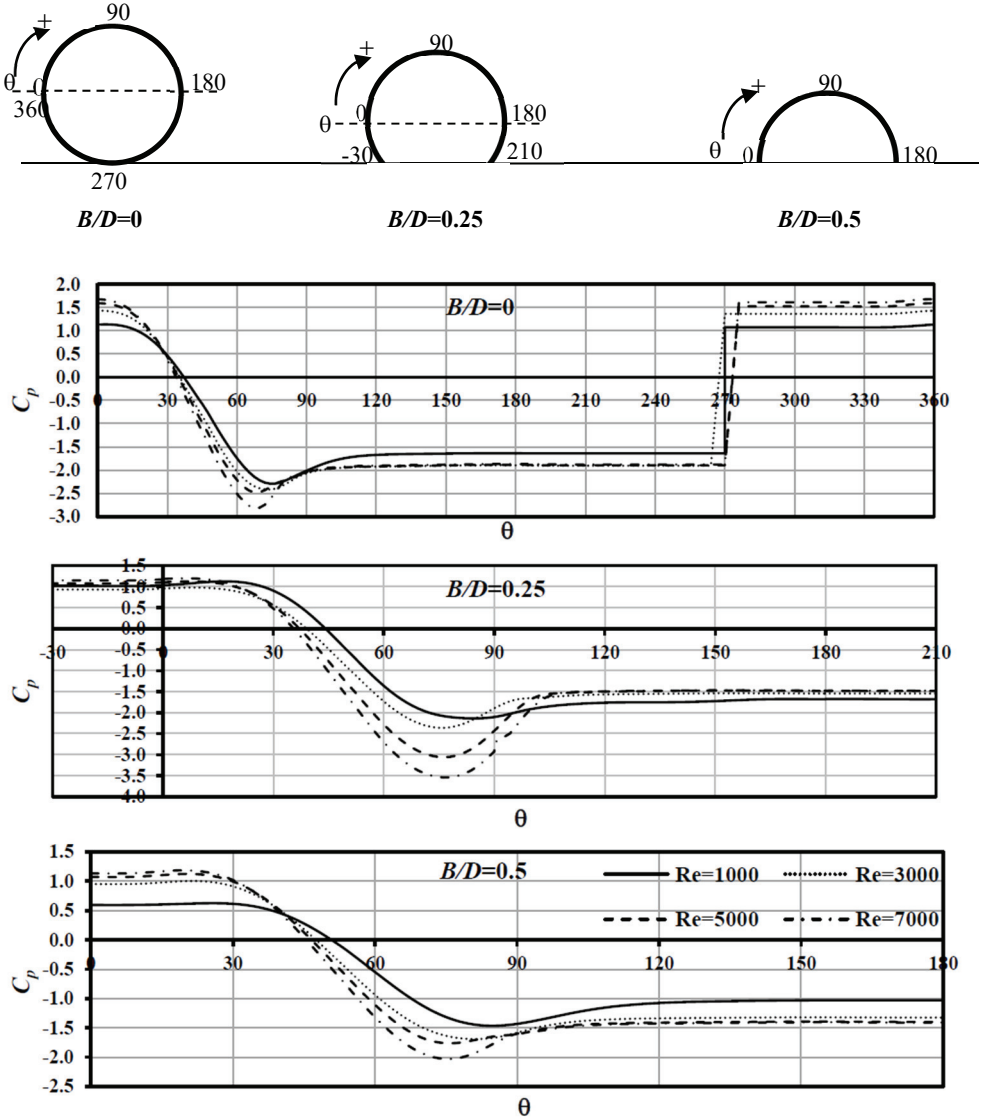
Figure 10 - Pressure coefficient distribution on the cylinder for B/D=0, 0.25, and 0.5 at Reynolds numbers 1000≤Re_D≤7000

Figure 11 shows the computed values of mean drag coefficient ($\overline{C_d}$) and lift coefficient ($\overline{C_l}$), using SST turbulence model for *B/D*=0, 0.25 and 0.5 at Reynolds numbers between Re_D=1000 and 7000. $\overline{C_d}$ values for *B/D*=0 are markedly greater than the values for the burial ratios of *B/D*=0.25 and 0.5. $\overline{C_d}$ tends to decrease with increasing of the Reynolds numbers. In addition, $\overline{C_d}$ decreases as the burial ratio increases. This can also be seen from the Table 6 which shows the $\overline{C_d}$ and $\overline{C_l}$ values for the different Re_D and *B/D* obtained by SST and DES models. The mean lift coefficients decrease with increasing of the Reynolds numbers. As may be also seen from Table 6, $\overline{C_l}$ decreases as the burial ratio increases.
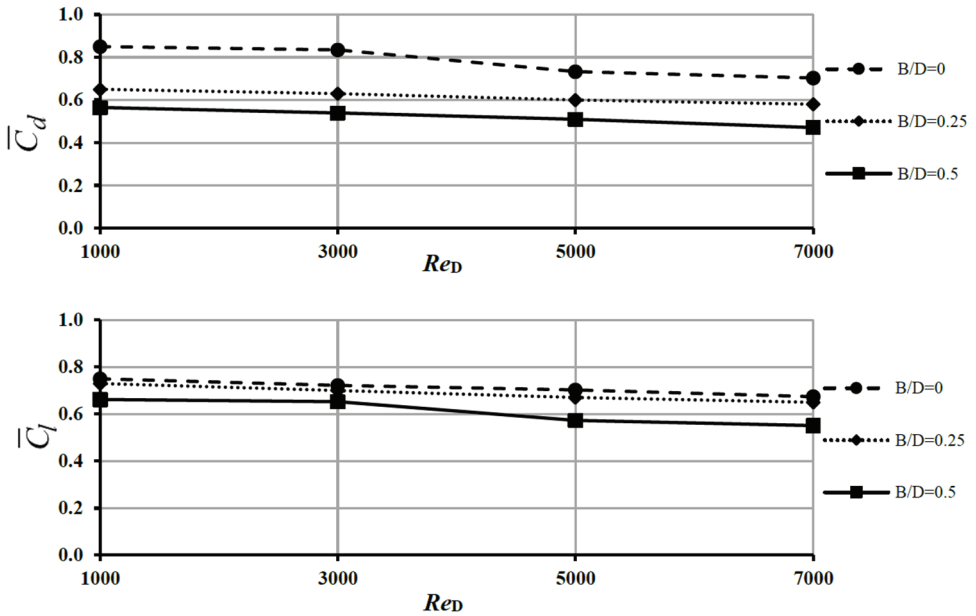
Figure 11 - Calculated mean drag ($\overline{C_d}$) and lift ($\overline{C_l}$) by SST turbulence model for B/D=0, 0.25 and 0.5 at Reynolds numbers in the ranges of 1000≤Re_D≤7000

Table 6 - The values of predicted mean drag and lift coefficients by SST and DES models for B/D=0, 0.25 and 0.5 at Reynolds numbers in the ranges of 1000≤Re_D≤7000

	$\overline{C_d}$-RANS			
B/D	Re_D=1000	Re_D=3000	Re_D=5000	Re_D=7000
0	0.850	0.835	0.733	0.703
0.25	0.650	0.630	0.600	0.580
0.5	0.565	0.540	0.509	0.471

Table 6 - The values of predicted mean drag and lift coefficients by SST and DES models for B/D=0, 0.25 and 0.5 at Reynolds numbers in the ranges of 1000≤Re$_D$≤7000 (continue)

$\overline{C_d}$-DES				
B/D	**Re$_D$=1000**	**Re$_D$=3000**	**Re$_D$=5000**	**Re$_D$=7000**
0	1.080	0.998	0.901	0.888
0.25	0.860	0.782	0.718	0.686
0.5	0.670	0.525	0.461	0.429
$\overline{C_l}$-RANS				
B/D	**Re$_D$=1000**	**Re$_D$=3000**	**Re$_D$=5000**	**Re$_D$=7000**
0	0.750	0.722	0.703	0.674
0.25	0.730	0.700	0.670	0.650
0.5	0.662	0.652	0.573	0.551
$\overline{C_l}$-DES				
B/D	**Re$_D$=1000**	**Re$_D$=3000**	**Re$_D$=5000**	**Re$_D$=7000**
0	0.957	0.929	0.899	0.802
0.25	0.860	0.800	0.766	0.740
0.5	0.755	0.740	0.728	0.706

The numerical results of drag and lift coefficients in this study are consistent with the measurements of the earlier researchers. Zdravkovich [29], found that the value of drag coefficient was 0.86 for *B/D*=0 at *Re*$_D$=8000. Kalghatgi and Sayer [30] reported that C_d was equal to 0.80 for *B/D*=0 at *Re*$_D$=10000. Cokgor and Avci [28] presented graphically the variation of drag and lift coefficient with the burial ratio and they reported that the drag and lift coefficient decreased with increasing burial ratio. The variation of the drag and lift coefficient with the burial ratio obtained from the studies mentioned above and the present numerical model is shown in Figures 12 and 13. The discrepancies from the previous studies in the literature could result from different flow and structure conditions. There are discrepancies in the RANS results, so the numerical analyses were reperformed by using DES (detached eddy simulation) model in two (2D) and three (3D) dimensional and LES models. The results obtained from 3D and 2D DES model are very compatible with each other. That's why the analyses for *B/D*=0, 0.25 and 0.5 at Reynolds numbers between *Re*$_D$=1000 and 7000 were carried out in 2D by using DES model. From the comparison of DES results with Cokgor and Avci [28] at Re=8000, it is obtained that the force coefficients are more compatible with each other according the RANS model results. Looking at Figures, it can be seen that numerical mean drag and lift coefficient distributions are very similar to those of experimental measurements.
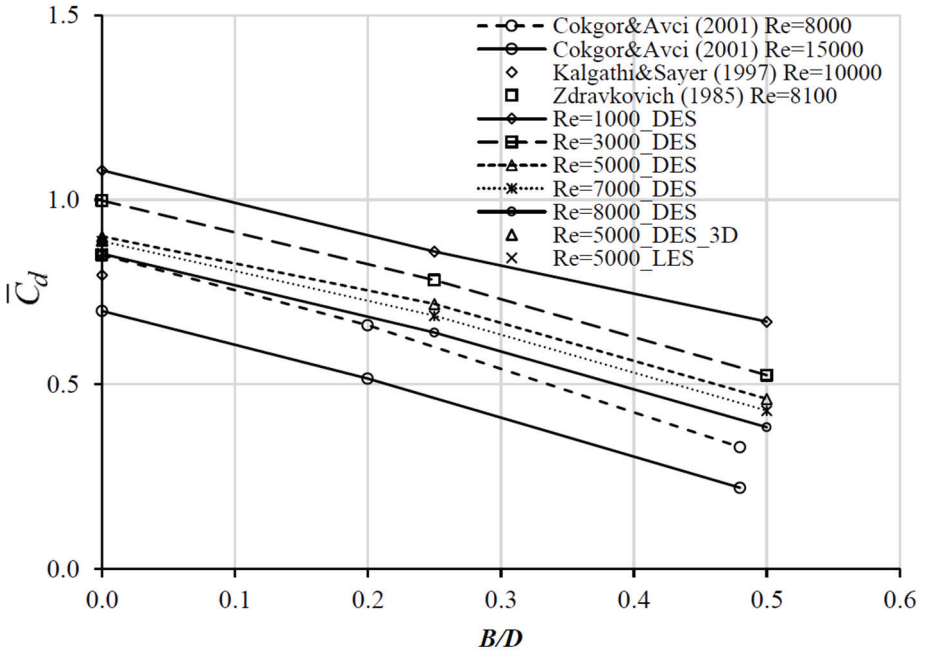
Figure 12 - Drag coefficient vs. burial ratio, B/D, for the different Re_D number
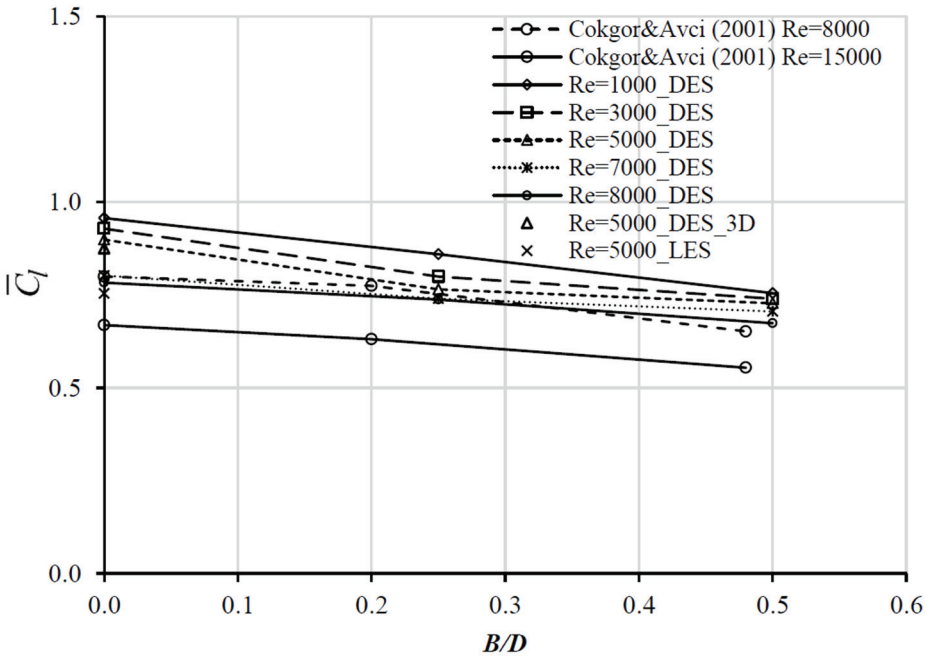
Figure 13 - Lift coefficient vs. burial ratio, B/D, for the different Re_D number

4.4. Experimental and numerical turbulence kinetic energy distributions

Figure 14 shows the comparison of turbulence kinetic energy (TKE), that is the rate at which energy is transferred from the main flow to the turbulent eddies, obtained from PIV and predicted using SST model at Re_D ranging from $1000 \leq Re_D \leq 7000$ for B/D=0.5. Maximum and incremental values of the turbulent kinetic energy are given in the figures. The distributions of TKE obtained from PIV and SST turbulence model are similar for all Reynolds numbers. It can be clearly seen that the maximum value of the turbulence kinetic energy is increasing with the increase of Reynolds number for both PIV and SST. A cluster and maximum value of TKE occur along the shedding shear layers.
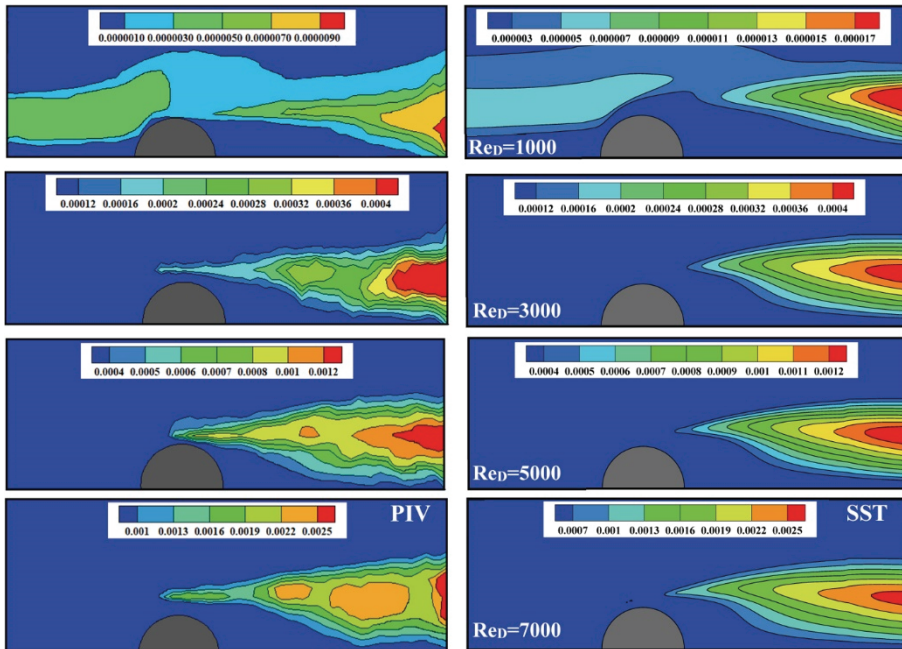
Figure 14 - Experimental and numerical turbulent kinetic energy for B/D=0.5

5. CONCLUSIONS

Analysis of the hydrodynamic behavior of the turbulent flow around a pipeline is important for the understanding of processes of scouring and self-burial of the pipelines governed by various mechanisms. To investigate the characteristics of the complex turbulent flow around the cylinder with different burial ratios at Reynolds number based on the cylinder diameter ranging from $1000 \leq Re_D \leq 7000$, the numerical simulation conducted using the Ansys-Fluent package program based on finite volume method. Standard k-ε, Renormalized Group k-ε, Realizable k-ε, Modified k-ω, Shear Stress Transport k-ω and Reynolds Stress Model turbulence models were employed to close the system of equations. Predicted velocity profiles were compared with those measured in laboratory using Particle Image Velocimetry.

The mean absolute relative error statistics were used as a criterion for the quantitative analysis of numerical results obtained from the turbulence closure models. From the comparisons of the numerical and experimental results, the simulation using SST model were found generally more accurate than other models. The pressure (C_p), mean drag ($\overline{C_d}$) and mean lift ($\overline{C_l}$) coefficients were predicted with SST turbulence model and DES model for the burial ratio *B/D*=0, 0.25 and 0.5 at Reynolds numbers in the range of 1000≤Re$_D$≤7000 and it was found that the force coefficients from the present computations were consistent with the measurements of the earlier researcher. Drag ($\overline{C_d}$) and lift ($\overline{C_l}$) coefficients decrease as the burial ratio increases. Turbulent kinetic energy obtained from PIV and SST turbulence model was increased with increasing Reynolds number and it concentrated along the shedding shear layers from the cylinder in which high velocity gradients occurred.

References

[1]   Sumer, B., and Fredsoe, J., Self-Burial of Pipelines at Span Shoulders, International Journal of Offshore and Polar Engineering, 4, 1, 1994.

[2]   Bearman, P., and Zdravkovich, M., Flow Around a Circular Cylinder Near a Plane Boundary, Journal of Fluid Mechanics, 89, 1, 33-47, 1978.

[3]   Zdravkovich, M., Aerodynamics of Two Parallel Circular Cylinders of Finite Height at Simulated High Reynolds Numbers, Journal of Wind Engineering and Industrial Aerodynamics, 6, 1-2, 59-71, 1980.

[4]   Fredsøe, J., and Hansen, E. A., Lift Forces on Pipelines in Steady Flow, Journal of Waterway, Port, Coastal, and Ocean Engineering, 113, 2, 139-155,1987.

[5]   Lei, C., Cheng, L., and Kavanagh, K., Re-Examination of the Effect of a Plane Boundary on Force and Vortex Shedding of a Circular Cylinder, Journal of Wind Engineering and Industrial Aerodynamics, 80, 3, 263-286, 1999.

[6]   Price, S., Sumner, D., Smith, J., Leong, K., and Paidoussis, M., Flow Visualization around a Circular Cylinder Near to a Plane Wall, Journal of Fluids And Structures, 16, 2, 175-191, 2002.

[7]   Oner, A. A., Kirkgoz, M. S., and Akoz, M. S., Interaction of a Current with a Circular Cylinder near a Rigid Bed, Ocean Engineering, 35, 14, 1492-1504, 2008.

[8]   Akoz, M. S., Flow Structures Downstream of the Horizontal Cylinder Laid on a Plane Surface, Proceedings of The Institution of Mechanical Engineers, Part C: Journal of Mechanical Engineering Science, 223, 2, 397-413,2009.

[9]   Aköz, M. S., Investigation of Vortical Flow Characteristics around a Partially Buried Circular Cylinder, Ocean Engineering, 52, 35-51, 2012.

[10]   Olsen, N. R., and Kjellesvig, H. M., Three-Dimensional Numerical Flow Modeling for Estimation of Maximum Local Scour Depth, Journal of Hydraulic Research, 36, 4, 579-590, 1998.

[11] Liang, D., Cheng, L., and Li, F., Numerical Modeling of Flow and Scour Below a Pipeline in Currents: Part II. Scour Simulation, Coastal Engineering, 52, 1, 43-62, 2005.

[12] Zhao, Z. H., and Fernando, H. J. S., Numerical Simulation of Scour around Pipelines Using an Euler-Euler Coupled Two-Phase Model, Environmental Fluid Mechanics, 7, 2, 121-142, 2007.

[13] Mao, Y., The interaction between a pipeline and an erodible bed, Series Paper Technical University of Denmark, 39, 1987.

[14] Kirkgoz, M. S., Oner, A. A., and Akoz, M. S., Numerical Modeling of Interaction of a Current with a Circular Cylinder Near a Rigid Bed, Advances in Engineering Software, 40, 11, 1191-1199, 2009.

[15] Akoz, M. S., and Kirkgoz, M. S., Numerical and Experimental Analyses of the Flow around a Horizontal Wall-Mounted Circular Cylinder, Transactions of the Canadian Society for Mechanical Engineering, 33, 2, 189-215, 2009.

[16] Dixen, M., Sumer, B. M., and Fredsoe, J., Numerical and Experimental Investigation of Flow and Scour around a Half-Buried Sphere, Coastal Engineering, 73, 84-105, 2013.

[17] Zhu, H., Qi, X., Lin, P., and Yang, Y., Numerical Simulation of Flow around a Submarine Pipe with a Spoiler and Current-Induced Scour Beneath the Pipe, Applied Ocean Research, 41, 87-100, 2013.

[18] Launder, B. E., and Spalding, D. B., Lectures in Mathematical Models of Turbulence, Academic Press, London, 1972.

[19] Yakhot, V., Orszag, S. A., Thangam, S., Gatski, T. B., and Speziale, C. G., Development of Turbulence Models for Shear Flows by a Double Expansion Technique. Physics of Fluids a-Fluid Dynamics, 4, 7, 1510-1520, 1992.

[20] Shih, T. H., Liou, W. W., Shabbir, A., Yang, Z. G., and Zhu, J., A New Kappa-Epsilon Eddy Viscosity Model for High Reynolds-Number Turbulent Flows. Computers & Fluids, 24, 3, 227-238, 1995.

[21] Wilcox, D. C., Turbulence Modeling for CFD, DCW Industries, Inc., California, 1998.

[22] Menter, F. R., 2-Equation Eddy-Viscosity Turbulence Models for Engineering Applications. AIAA Journal, 32, 8, 1598-1605, 1994.

[23] Launder, B. E., Reece, G. J., and Rodi, W., Progress in the Development of a Reynolds-Stress Turbulence Closure, Journal of Fluid Mechanics, 68, 3, 537-566, 1975.

[24] Wolfshtein, M., The Velocity and Temperature Distribution in One-Dimensional Flow with Turbulence Augmentation and Pressure Gradient, International Journal of Heat and Mass Transfer, 12, 3, 301-318, 1969.

[25] Kirkgoz, M. S., and Ardiclioglu, M,. Velocity Profiles of Developing and Developed Open Channel Flow, Journal Hydraulic Engineering-ASCE, 123, 12, 1099-1105, 1997.

[26] Ansys Fluent User Guide, Ansys Inc., 2012.

[27] Roache, P. J., Verification of Codes and Calculations, AIAA Journal, 36, 5, 696-702, 1998.

[28] Cokgor, S., and Avci, I., Hydrodynamic Forces on Partly Buried Tandem, Twin Pipelines in Current, Ocean Engineering, 28, 10, 1349-1360, 2001.

[29] Zdravkovich, M., Flow Induced Oscillations of Two Interfering Circular Cylinders, Journal of Sound and Vibration, 101, 4, 511-521, 1985.

[30] Kalghatgi, S., and Sayer, P., Hydrodynamic Forces on Piggyback Pipeline Configurations, Journal of waterway, port, coastal, and ocean engineering, 123, 1, 16-22, 1997.